Rashba exciton in a 2D perovskite quantum dot

Journal Name

ARTICLE TYPE

Rashba exciton in a 2D perovskite quantum dot[†]

Michael W. Swift,[a‡] John L. Lyons,[a] Alexander L. Efros,[a*], and Peter C. Sercel[b,c*]

The Rashba effect has been proposed to give rise to a bright exciton ground state in halide perovskite nanocrystals (NCs), resulting in very fast radiative recombination at room temperature and extremely fast radiative recombination at low temperature. In this paper we find the dispersion of the "Rashba exciton", i.e., the exciton whose bulk dispersion reflects large spin-orbit Rashba terms in the conduction and valence bands and thus has minima at non-zero quasi-momenta. Placing Rashba excitons in quasi-2D cylindrical quantum dots, we calculate size-dependent levels of confined excitons and their oscillator transition strengths. We consider the implications of this model for two-dimensional hybrid organic-inorganic perovskites, and discuss generalizations of this model to 3D NCs.

After 25 years of study of various semiconductor nanostructures started by the investigation of the exciton fine structure in CdSe nanocrystals (NCs)[1] there is a common belief that the ground exciton state is always dark (i.e., optically inactive). However 6 years ago it was discovered that the radiative decay time in certain halide perovskite NCs was surprisingly short[2] and became even shorter with decreasing temperature.[3] To explain these unexpected results it was suggested that the ground exciton state is an optically active bright exciton, which could be realized in perovskite NCs in the presence of large Rashba spin-orbit terms.[4] Measurements of picosecond-scale dephasing times of the bright triplet fine structure levels in $CsPbI_3$ NCs[5] are consistent with this picture, while other studies have called the suggestion into question, proposing that the ground state in these systems is not bright, but instead that relaxation into the dark ground state is restricted by a phonon bottleneck.[6,7] Regardless of the nature of the ground state in this particular example, it is well established theoretically that the Rashba effect gives rise to an important effective electron-hole exchange interaction which could in principle lead to a bright-dark level inversion.[8,9]

Since a bright ground exciton state would lead to excellent optoelectronic properties,[4,8,9] the possibility of a Rashba-mediated bright-dark level inversion in other systems must be explored. The two-dimensional hybrid organic-inorganic perovskites (2D HOIPs) are fruitful ground for this investigation, since very large Rashba coefficients have been measured[10,11] or computationally predicted[12–14] in these materials. A 2D HOIP quantum dot would be particularly promising for fast radiative recombination, since confinement will lead to large exciton binding energies[15] and giant oscillator transition strengths.[16] We therefore construct an effective-mass model of excitons in this system.

Measured Rashba terms in 2D HOIPs are sufficiently large that advances in exciton modeling are required to describe them correctly. Previous theoretical descriptions of Rashba terms in exciton fine structure were conducted in the weak-confinement regime, in which the exciton Bohr radius, a_B, is much smaller than the typical size of the NC.[4] The Rashba effect was treated perturbatively, which is a valid approach assuming $\alpha_{e,h}K \ll \hbar^2 K^2/2M$, where α_e and α_h are the Rashba coefficients in the conduction and valence bands respectively, K is the typical quasi-momentum of exciton center-of-mass (COM) motion, and $M = m_e + m_h$ is the effective mass of the COM motion, equal to the sum of the electron, m_e, and hole, m_h, effective masses. The momentum $K \sim 1/R$ for an exciton confined in a NC with size R, so the perturbative approach is valid when $\alpha_{e,h} \ll \hbar^2/2MR$. This condition is clearly not satisfied in large NC ($R \gg \hbar^2/2M\alpha_{e,h}$) or in NCs with enormously large Rashba coefficients. For these cases, it is necessary to go beyond the perturbative approach.

In this paper we develop a theory which covers the full range of NC sizes and Rashba strengths. The theory describes the "Rashba exciton", i.e., the exciton whose bulk dispersion includes the effect of α_e and α_h non-perturbatively and thus has a Rashba-like form as shown in Figure 1. The size dependence of the Rashba exciton fine structure and the relative oscillator transition strengths are calculated within a quasi-two-dimensional (2D) quantum dot

* Corresponding authors. Email: sasha.efros@nrl.navy.mil, psercel@caltech.edu
a Center for Computational Materials Science, U.S. Naval Research Laboratory, Washington D.C. 20375, United States
b Department of Applied Physics and Materials Science, California Institute of Technology, Pasadena, California 91125, United States
c Center for Hybrid Organic Inorganic Semiconductors for Energy, Golden, Colorado 80401, United States

model. Numerical results are calculated using parameters chosen to correspond roughly to 2D HOIPs, whose Rashba coefficients are very large and have been measured.[10,11] The model can be applied to a wide variety of systems through an appropriate choice of parameters, facilitated by the provided python implementation of the Rashba exciton model.[†] Implications for optoelectronic devices based on 2D HOIPs are discussed, as well as the possible extension of the developed results to three-dimensional NCs.
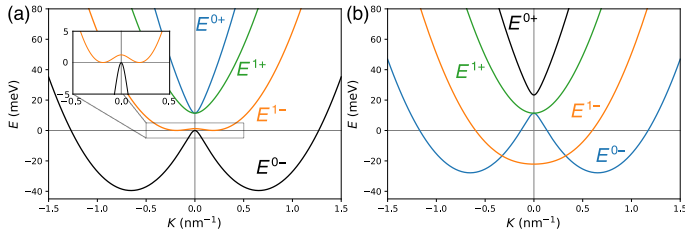

Fig. 1 Dispersion of the Rashba exciton in a 2D layer having tetragonal crystal symmetry and broken inversion symmetry in the out-of-plane direction. In panel (a) the effect of the electron and hole Rashba terms on exciton internal motion is not taken into account, while panel (b) does include this effect. In panel (a) the E^{0-} level (shown in black) corresponds to the dark (optically passive) level at $K = 0$, while other levels shown in panel (a) are bright (optically active). E^{0+} is shown in blue, E^{1+} in green, and E^{1-} in orange. The inset in panel (a) shows a magnified view of the dispersion near the origin, highlighting the gap between E^{0-} and E^{-1} at $K = 0$. In panel (b) the E^{0-} now corresponds to an optically active level at $K = 0$ and is thus shown in blue, while E^{0+} is the optically passive (dark) state at $K = 0$, and is thus shown in black (see Eq. (16)). As in panel (a), E^{1+} is shown in green and E^{1-} in orange. Note that the effective exchange due to the Rashba term in panel (b) inverts the bright-dark level ordering at $K = 0$ so the ground state is bright, but the global ground state is an indirect ($K \neq 0$) dark exciton. Eq. (16) describes the exciton dispersion, and the parameters used in this plot are in Table 1.

1 Dispersion of the 2D Rashba exciton

The free exciton Hamiltonian in semiconductors with parabolic conduction and valence bands allows separation of variables, and can be written as a sum of COM and relative motion terms,

$$\hat{H}_0 = \hat{H}_{0,\text{COM}} + \hat{H}_{0,\text{REL}} = \frac{\hat{\boldsymbol{P}}^2}{2M} + \left[\frac{\hat{\boldsymbol{p}}^2}{2\mu} + V(|\boldsymbol{r}|) \right] . \quad (1)$$

These coordinates are defined in terms of electron and hole coordinates in the usual way: $\boldsymbol{r} = \boldsymbol{r}_e - \boldsymbol{r}_h$, $\hat{\boldsymbol{P}} = \hat{\boldsymbol{p}}_e + \hat{\boldsymbol{p}}_h$, $\hat{\boldsymbol{p}} = (m_h \hat{\boldsymbol{p}}_e - m_e \hat{\boldsymbol{p}}_h)/M$, and $\mu = (1/m_e + 1/m_h)^{-1}$.[8] In organic-inorganic metal halide perovskites it has been reported that the inversion symmetry perpendicular to the 2D or quasi-2D layer is broken.[10] Due to the strong spin-orbit coupling in metal halide perovskite semiconductors, the broken inversion symmetry generates Rashba terms that are linear in the electron and hole momenta. Putting the z axis in the direction perpendicular to the 2D layer, we can also write Rashba term contributions as a sum of a COM term $\hat{H}_{R,\text{COM}}$

and a relative term $\hat{H}_{R,\text{REL}}$:[17]

$$\hat{H}_{R,\text{COM}}(\boldsymbol{P}) = \frac{1}{M} \left[\left(m_e \frac{\alpha_{xy}^e}{\hbar} \hat{j}_x^e + m_h \frac{\alpha_{xy}^h}{\hbar} \hat{j}_x^h \right) P_y \right.$$

$$\left. - \left(m_e \frac{\alpha_{yx}^e}{\hbar} \hat{j}_y^e + m_h \frac{\alpha_{yx}^h}{\hbar} \hat{j}_y^h \right) P_x \right] , \quad (2)$$

$$\hat{H}_{R,\text{REL}} = \left(\frac{\alpha_{xy}^e}{\hbar} \hat{j}_x^e - \frac{\alpha_{xy}^h}{\hbar} \hat{j}_x^h \right) \hat{p}_y - \left(\frac{\alpha_{yx}^e}{\hbar} \hat{j}_y^e - \frac{\alpha_{yx}^h}{\hbar} \hat{j}_y^h \right) \hat{p}_x , \quad (3)$$

where $\alpha_{xy}^e, \alpha_{yx}^e$ and $\alpha_{xy}^h, \alpha_{yx}^h$ are the Rashba coefficients for electrons and holes in perovskites with orthorhombic crystal structures, respectively, and $\hat{j}_x^e, \hat{j}_y^e$ and $\hat{j}_x^h, \hat{j}_y^h$ are Pauli operators representing the electron and hole angular momentum projections along x, y. For tetragonal symmetry, the Rashba coefficients associated with motion along the two in-plane directions are equal: $\alpha_{xy}^{e,h} = \alpha_{yx}^{e,h}$.

1.1 Exciton relative motion terms

The $\hat{H}_{R,\text{REL}}$ contribution of the Rashba terms was shown to affect exciton fine structure and even can change the order of bright and dark exciton levels.[4] As was written above, these terms in Ref. 4 were treated perturbatively, leading to an effective electron-hole exchange interaction. If the inversion asymmetry is taken along the z direction,

$$\hat{H}_{\text{exch}}^{\text{REL}} = -A_R \left(\frac{m_e m_h}{M \hbar^2} \right) \left[(\alpha_{yx}^e \hat{j}_y^e - \alpha_{yx}^h \hat{j}_y^h)^2 + (\alpha_{xy}^e \hat{j}_x^e - \alpha_{xy}^h \hat{j}_x^h)^2 \right] , \quad (4)$$

where A_R is a numerical factor whose value depends on the exciton dimensionality. In the 2D hydrogenic limit Sercel found that in the absence of dielectric confinement effects $A_R^{2D} = \left(\frac{3\sqrt{3}}{16} \right)^2 \sim 0.105$.[18] In layered perovskite structures, however, the 2D semiconductor layer is surrounded by media with a different dielectric constant. The numerical coefficient $A_R^{\mathscr{L}}$ depends on the layer thickness $\mathscr{L}$ and on the ratio $\kappa = \varepsilon_i/\varepsilon_o$ of the dielectric constants of the semiconductor layer (ε_i) and the surrounding media (ε_o). This is because the internal motion of the exciton is modified by dielectric confinement, resulting in a modified electron-hole interaction potential.[19,20] We describe this modified potential using the image charge method introduced by Hanamura et al.[21] and previously utilized to calculate exciton binding energies in layered 2D HOIPs by Hong et al..[22] In terms of the relative radial coordinate of the electron and hole in the plane, $\rho_{e,h}$, and the z-coordinates z_e, z_h of the electron and hole, the interaction potential can be written in CGS units,

$$V_{eh}^{3D}(\rho, z_e, z_h) = -\frac{e^2}{\varepsilon_i} \sum_{n=-\infty}^{n=\infty} \frac{q_n}{\sqrt{\rho_{e,h}^2 + (z_e - z_{h,n})^2}} , \quad (5)$$

where $q_n = q_{-n} = [(\kappa - 1)/(\kappa + 1)]^{|n|}$ and $z_{h,n} = (-1)^{|n|} z_h + n\mathscr{L}$.

In Ref. 23 the ground state $(n, m) = (1, 0)$ wavefunctions were found variationally using the 2D hydrogenic ansatz[24]: $\phi_{1,0}(\rho_{e,h}; a_{1,0}) \sim \exp(-2\rho_{e,h}/a_{1,0})$, where $a_{1,0}$ is the variational parameter, and the wavefunction $2/\mathscr{L} \cos(\pi z_e/\mathscr{L}) \cos(\pi z_h/\mathscr{L})$ de-

scribes electron and hole confinement in the layer. We extend this methodology to the excited state $(n,m) = (2,\pm1)$ using $\phi_{2,\pm1}(\rho_{e,h},\phi;a_{2,1}) \sim \rho_{e,h}\exp(-2\rho_{e,h}/3a_{2,1})\exp(\pm i\phi)$ with the variational parameter $a_{2,1}$, as shown in Fig. S-1 in the ESI. Following the approach suggested in Ref. 4 and taking into account the different radii $a_{1,0}$ and $a_{2,\pm1}$, we obtain the numerical coefficient:

$$A_R^{\mathscr{L}} = 4a_{1,0}^2 \frac{384a_{1,0}^2 a_{2,\pm1}^2}{(a_{1,0}+3a_{2,\pm1})^6}\left[\frac{\hbar^2/(2\mu a_{1,0}^2)}{E_{1,0}(a_{1,0})-E_{2,\pm1}(a_{2,\pm1})}\right] . \quad (6)$$

In the 2D limit with no dielectric discontinuity, the range parameters $a_{1,0} = a_{2,\pm1} = a_x$, where a_x is the 3D bulk exciton radius. In that case, the energies $E_{1,0} = -4[\hbar^2/(2\mu a_x^2)]$ and $E_{2,\pm1} = -4/9[\hbar^2/(2\mu a_x^2)]$ and Eq. (6) reduces to the idealized 2D case. This limit is verified numerically and the dependence on κ is explored in ESI Fig. S-1.

We note that Eq. (5) assumes an infinite dielectric outside the semiconducting layer. Strictly speaking, this would correspond to an exfoliated single layer of a 2D HOIP, whereas for a stacked HOIP sample, a "dielectric superlattice" model would be more appropriate.[25] Our calculated binding energy (415 meV) is in good agreement with previous results for an exfoliated single layer based on a semi-empirical tight-binding approach[26], as well as previous magneto-absorption measurements and effective-mass theory[27]. A superlattice model would result in a smaller binding energy (200-300 meV) and larger exciton radii.[26]

With $A_R^{\mathscr{L}}$ in hand, we can proceed to calculate the internal Rashba terms. Assuming that the 2D layer has symmetry higher than orthorhombic gives us $\alpha_{yx}^e = \alpha_{xy}^e \equiv \alpha_e$ and $\alpha_{yx}^h = \alpha_{xy}^h \equiv \alpha_h$. Using these definitions we can rewrite the term in square brackets within Eq. (4) as a sum of three terms: $\alpha_e^2(3/4 - \hat{j}_z^{e2}) + \alpha_h^2(3/4 - \hat{j}_z^{h2}) + 2\alpha_e\alpha_h(\hat{j}_x^e\hat{j}_x^h + \hat{j}_y^e\hat{j}_y^h)$. Ignoring the first two terms which give an angular momentum-independent energy offset $\Delta E \sim (\alpha_e^2 + \alpha_h^2)$, we obtain the effective exchange Hamiltonian,

$$\hat{H}_{\text{exch}}^{\text{REL}} = 2A_R\mathscr{E}_R\left(\hat{j}_x^e\hat{j}_x^h + \hat{j}_y^e\hat{j}_y^h\right) , \quad (7)$$

where $\mathscr{E}_R = \alpha^e\alpha^h\mu/\hbar^2$ is the exciton Rashba energy.[8,9]

The operator $\hat{H}_{\text{exch}}^{\text{REL}}$ in the exciton Bloch function total angular momentum basis $|J,J_z\rangle$, taken in the order, $|0,0\rangle$, $|1,1\rangle$, $|1,0\rangle$, $|1,-1\rangle$ can be written

$$\bar{H}_{\text{exch}}^{\text{REL}} = 4A_R\mathscr{E}_R\begin{pmatrix} -1 & 0 & 0 & 0 \\ 0 & 0 & 0 & 0 \\ 0 & 0 & 1 & 0 \\ 0 & 0 & 0 & 0 \end{pmatrix} . \quad (8)$$

The effective exchange term in Eq. (8) can be added to the short-range exchange interaction in a 2D system that has been previously derived.[8,9,17,28–31] The transformation from the electron-hole pair basis from Refs. 8,9,23 to the angular momentum basis $|J,J_z\rangle$ basis we used for the effective Rashba exchange is given in Eq. (S1) (equation numbers beginning with S may be found in the ESI). This results in the short-range exchange eigenvalues E_{J,J_z} for the state J,J_z as follows: $E_{0,0} = E_d = 0$, $E_{1,\pm1} = E_t = w\cos^2\theta$, and $E_{1,0} = E_z = 2w\sin^2\theta$, where w is the short-range exchange constant and θ is the crystal field phase an-

gle[8] (See Table 1). Therefore the combined effect of SR exchange splitting and the internal motion Rashba terms above is:

$$E_{0,0} = E_d = -4A_R\mathscr{E}_R, \qquad E_{1,0} = E_z = 2w\sin^2\theta + 4A_R\mathscr{E}_R,$$

$$E_{1,1} = E_{1,-1} = E_t = w\cos^2\theta \quad (9)$$

We see that with electron and hole Rashba coefficients α_e and α_h of opposite sign, $\mathscr{E}_R < 0$ and the dark state shifts *upwards* in energy.

1.2 Exciton center of mass terms

The Rashba terms in the conduction and valence bands lead to additional fine structure connected with the exciton center of mass motion, described by the Hamiltonian $\hat{H}^{\text{COM}}(\boldsymbol{K})$, where $\boldsymbol{K} = \boldsymbol{P}/\hbar$, can be written as[17]

$$\hat{H}^{\text{COM}}(\boldsymbol{K}) = \frac{1}{M}(m_e\alpha_e[\hat{\boldsymbol{j}}_e \times \boldsymbol{K}] + m_h\alpha_h[\hat{\boldsymbol{j}}_h \times \boldsymbol{K}])\cdot\boldsymbol{n} , \quad (10)$$

where $\boldsymbol{n}$ is the unit vector that defined the direction of the inversion asymmetry, here assumed to be directed perpendicular to the 2D perovskite layer. Using Eq. (10) we can write the effective Bloch-angular-momentum-dependent Hamiltonian associated with free exciton center-of-mass motion in the plane-wave basis. Representing Eq. (10) in a basis of the four conduction and valence band Bloch function products, $|c_1\rangle|v_1\rangle$, $|c_1\rangle|v_2\rangle$, $|c_2\rangle|v_1\rangle$ and $|c_2\rangle|v_2\rangle$ and using the transformation matrix given in Eq. (S1) we arrive at,

$$\hat{H}_{\text{COM},J}^{\text{Tetr}}(\boldsymbol{K}) = \frac{1}{\sqrt{2}}\begin{pmatrix} 0 & -iK_+\alpha_{\text{ex}}^- & 0 & -iK_-\alpha_{\text{ex}}^- \\ iK_-\alpha_{\text{ex}}^- & 0 & iK_-\alpha_{\text{ex}}^+ & 0 \\ 0 & -iK_+\alpha_{\text{ex}}^+ & 0 & iK_-\alpha_{\text{ex}}^+ \\ iK_+\alpha_{\text{ex}}^+ & 0 & -iK_+\alpha_{\text{ex}}^+ & 0 \end{pmatrix}, \quad (11)$$

where $\alpha_{\text{ex}}^\pm = (\alpha_e m_e \pm \alpha_h m_h)/M$ and $K_\pm = K_x \pm iK_y$. We note that, with non-zero momentum, the dark $|0,0\rangle$ state must be mixed with the upper bright $|1,0\rangle$ and $|1,\pm1\rangle$ states except in the unlikely special condition that $m_e\alpha = m_h\beta$.

A complete description of the exciton dispersion requires, however, that we also include the exciton fine structure splitting due to electron-hole exchange and the internal motion Rashba terms as described in Eq. (9), resulting in the following Hamiltonian:

$$\hat{H}_{\text{tot},J}^{\text{Tetr}}(\boldsymbol{K}) = \hat{H}_{\text{INT},J}^{\text{Tetr}} + \hat{H}_{\text{COM},J}^{\text{Tetr}}(\boldsymbol{K}) , \quad (12)$$

where $\hat{H}_{\text{INT},J}^{\text{Tetr}}$ describes the fine structure of the exciton connected with exciton internal motion at $K = 0$. As a result the total exciton dispersion is described as

$$\hat{H}_{\text{tot},J}^{\text{Tetr}}(\boldsymbol{K}) = \left[\mathscr{E}_{0,0} + \frac{\hbar^2K^2}{2M}\right]\mathbb{I} + \begin{pmatrix} E_d & 0 & 0 & 0 \\ 0 & E_t & 0 & 0 \\ 0 & 0 & E_z & 0 \\ 0 & 0 & 0 & E_t \end{pmatrix} +$$

$$\frac{i}{\sqrt{2}}\begin{pmatrix} 0 & -K_+\alpha_{\text{ex}}^- & 0 & -K_-\alpha_{\text{ex}}^- \\ K_-\alpha_{\text{ex}}^- & 0 & K_-\alpha_{\text{ex}}^+ & 0 \\ 0 & -K_+\alpha_{\text{ex}}^+ & 0 & K_-\alpha_{\text{ex}}^+ \\ K_+\alpha_{\text{ex}}^+ & 0 & -K_+\alpha_{\text{ex}}^+ & 0 \end{pmatrix}, \quad (13)$$

where $K^2 = K_x^2 + K_y^2$, $\mathbb{I}$ is the 4x4 unit matrix, and the internal fine structure energies E_d, E_t and E_z are given in Eq. (9).

The final missing piece is long-range exchange. The methodology for this calculation has been established,[23,32] but requires the form of the wavefunctions. This requires treatment of the 2D quantum well, which will be addressed in Section 2. We will return to the question of long-range exchange in Section 5.

2   Energy spectrum of the 2D Rashba exciton

To describe spectra of confined excitons in cylindrical quasi-2D QDs we need to separate the azimuthal and radial variables in the wavefunction of the exciton COM motion. The Hamiltonian describing the exciton COM in Eq. (13) conserves the total angular momentum in the direction perpendicular the plane of 2D layer: $F_z = J_z + \ell$, where ℓ is the envelope angular momentum. The dependence of the exciton wavefunction on COM coordinates ρ and ϕ can therefore be separated, and the angular part may be written down immediately. This leaves only the radial part $\mathscr{R}_{J,J_z}^{F_z}(\rho)$ unknown. The full wavefunction is

$$\Psi_{F_z}(\rho,\phi,\rho_{eh},z_e,z_h) = \frac{2}{\mathscr{L}}\cos\left(\frac{\pi z_e}{\mathscr{L}}\right)\cos\left(\frac{\pi z_h}{\mathscr{L}}\right)\phi_{m,n}(\rho_{eh})\times$$

$$\frac{\mathscr{N}}{\sqrt{2\pi}}\left[e^{iF_z\phi}\mathscr{R}_{0,0}^{F_z}(\rho)|0,0\rangle + \sum_{\mu=\pm1,0}e^{i(F_z-\mu)\phi}\mathscr{R}_{1,\mu}^{F_z}(\rho)|1,\mu\rangle\right],$$

(14)

where $\mathscr{N}$ is a normalization factor for the COM wavefunction, defined in Eq. (S46). Internal motion is included through the cosine terms, which represent electron and hole confinement in the layer, and the variationally determined wavefunction $\phi_{n,m}$ for the in-plane relative radial coordinate $\rho_{e,h}$ (see (5) and following).

As we show in Sec. S-II of the ESI, the resulting Hamiltonian matrix can be written in the product basis $|F_z\rangle = |J,J_z\rangle|F_z-J_z\rangle$, where $|J,J_z\rangle$ denotes the exciton Bloch function defined just before (8) while $|\ell\rangle = |F_z-J_z\rangle$ is the envelope function. The matrix representation of the Hamiltonian in this basis is,

$$\hat{H}_{F_z} = \begin{pmatrix} \mathscr{E}_{0,0}+\frac{\hbar^2K^2}{2M} & \frac{1}{\sqrt{2}}K\alpha_{\text{ex}}^- & 0 & -\frac{1}{\sqrt{2}}K\alpha_{\text{ex}}^- \\ \frac{1}{\sqrt{2}}K\alpha_{\text{ex}}^- & \mathscr{E}_{0,0}+E_t+\frac{\hbar^2K^2}{2M} & \frac{1}{\sqrt{2}}K\alpha_{\text{ex}}^+ & 0 \\ 0 & \frac{1}{\sqrt{2}}K\alpha_{\text{ex}}^+ & \mathscr{E}_{0,0}+E_z+\frac{\hbar^2K^2}{2M} & \frac{1}{\sqrt{2}}K\alpha_{\text{ex}}^+ \\ -K\alpha_{\text{ex}}^- & 0 & \frac{1}{\sqrt{2}}K\alpha_{\text{ex}}^- & \mathscr{E}_{0,0}+E_t+\frac{\hbar^2K^2}{2M} \end{pmatrix}.$$

(15)

(column headers: $|0,0\rangle|F_z\rangle$ $|1,1\rangle|F_z-1\rangle$ $|1,0\rangle|F_z\rangle$ $|1,-1\rangle|F_z+1\rangle$)

The Hamiltonian can be decomposed into two 2x2 matrices by another change of basis given in Eq. (S15) and subsequently diagonalized analytically, giving the Rashba exciton dispersion:

$$E_{F_z}^{1\pm}(K) = \mathscr{E}_{0,0} + \frac{\hbar^2K^2}{2M} + \frac{E_t+E_z}{2} \pm \frac{\sqrt{(E_t-E_z)^2+4K^2(\alpha_{\text{ex}}^+)^2}}{2},$$

$$E_{F_z}^{0\pm}(K) = \mathscr{E}_{0,0} + \frac{\hbar^2K^2}{2M} + \frac{E_d+E_t}{2} \pm \frac{\sqrt{(E_d-E_t)^2+4K^2(\alpha_{\text{ex}}^-)^2}}{2}.$$

(16)

The same dispersion is found in the plane-wave basis by diagonalization of the plane-wave Hamiltonian, $\hat{H}_{\text{tot},F}^{\text{Tetr}}(\boldsymbol{K})$, Eq. (13). The

eigenvectors of Eq. (15) are:

$$\left|\boldsymbol{E}_{F_z}^{1\pm}\right\rangle = \frac{1}{\sqrt{1+c_{1\pm}^2(K)}}\begin{pmatrix} 0 \\ c_{1\pm}(K)/\sqrt{2} \\ 1 \\ c_{1\pm}(K)/\sqrt{2} \end{pmatrix},$$

$$\left|\boldsymbol{E}_{F_z}^{0\pm}\right\rangle = \frac{1}{\sqrt{1+c_{0\pm}^2(K)}}\begin{pmatrix} c_{0\pm}(K) \\ -1/\sqrt{2} \\ 0 \\ 1/\sqrt{2} \end{pmatrix},$$

(17)

where the c coefficients are given in Eq. (S3). These are the exciton states in an infinite 2D sheet not subject to lateral confinement. The expression for $\left|\boldsymbol{E}_{F_z}^{0\pm}\right\rangle$ in Eq. (17) shows that exciton center-of-mass motion mixes the dark $|0,0\rangle$ exciton state with bright $|1,\pm1\rangle$ exciton states.

An important feature of the Rashba exciton dispersion (16) is the density of states at low energy. The exciton has its minimum energy $\mathscr{E}_{\text{min}}$ on a circle in K-space defined by $K_x^2+K_y^2 = K_R^2$, where $\mathscr{E}_{\text{min}}$ and K_R are given in Eq. (S5). As a result, the density of states near the energy minimum has an effective one-dimensional character, diverging as $D(E) \propto (E-\mathscr{E}_{\text{min}})^{-1/2}$ (see Eqs. (S5-S9)). Due to this large density of states, we can expect an enhanced transition rate into states near the minimum, despite the K-indirect nature of these transitions. To quantify this intuition, we consider the rate of phonon-assisted absorption of a photon with energy $\hbar\omega$. Absorption from the ground state $|\mathscr{G}\rangle$ into the exciton state $|\psi\rangle$ with energy $E = \hbar\omega$ proceeds through an intermediate state $|\chi\rangle$ via an indirect phonon-assisted process. The transition rate is given by Fermi's golden rule:

$$\Gamma = \frac{2\pi}{\hbar}\left|\sum_\chi \frac{\langle\psi|H_{ex-ph}|\chi\rangle\langle\chi|H_{\boldsymbol{e}}|\mathscr{G}\rangle}{E_\chi-E}\right|^2 D(E),$$

(18)

where χ is a virtual optically active exciton state at $K = 0$, $\langle\chi|H_{\boldsymbol{e}}|\mathscr{G}\rangle$ is the dipole matrix element between $|\chi\rangle$ and $|\mathscr{G}\rangle$ for light with polarization $\boldsymbol{e}$, and $\langle\psi|H_{ex-ph}|\chi\rangle$ is the exciton-phonon matrix element between $|\chi\rangle$ and $|\psi\rangle$. While exciton-phonon interactions are beyond the scope of this work, the large density of states at $E = \mathscr{E}_{\text{min}}$ means that the absorption and emission rates for the indirect exciton at K_R may still be quite substantial.

3   The energy of confined levels

In this part of the paper we use the approach of Bulgakov and Sadreev[33] to find the energy levels of the confined exciton with dispersion given by Eq. (16). For a given exciton energy E, we can solve Eq. (16) to find four independent momenta $K_{1\pm}$ and $K_{0\pm}$, as shown in Eq. (S4). It is important to note that the $\pm$ signs in $K_{1\pm}$, $K_{0\pm}$ do not correspond to the $\pm$ signs in Eq. (16) for the exciton energy dispersion $E^{1\pm}$ and $E^{0\pm}$. A given energy E corresponds to K_{1+}^2 and K_{1-}^2 within the $E^{1\pm}$ branches, but they may both be from E^{1+}, both from E^{1-}, or one from each. The same is true for $K_{0\pm}^2$ and $E^{0\pm}$. This is illustrated in Figure 2, which shows E versus K^2 and the inverted K^2 vs E color-coded by branch. For example, consider $E = 0$ meV in panels (b) and (d). The two $K_{0\pm}^2$ are both from E^{0-}, K_{1+}^2 is from E^{1-}, and K_{1-}^2 corresponds to E^{1+}.
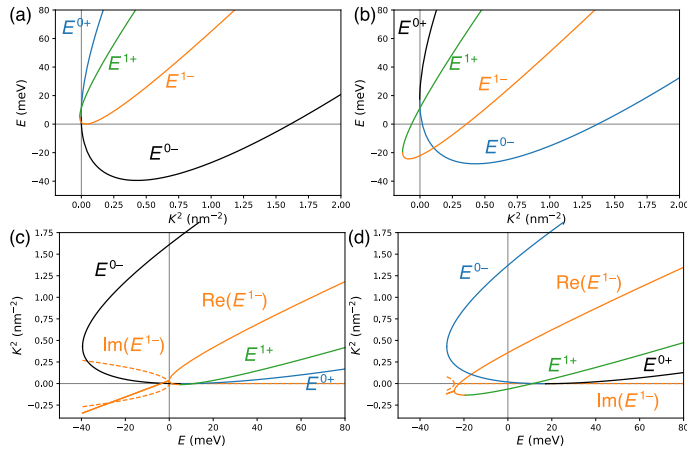
Fig. 2 (a) Energy E versus K^2 (see Fig. 1, Eq. (16)) with no internal Rashba and (b) with internal Rashba. (c) inverted dispersion, complex K^2 vs E, with no internal Rashba and (d) including internal Rashba. Real parts of K^2 are shown in solid lines, while non-zero imaginary parts are shown as dashed lines. In all panels, the lines are color-coded by E branch to match Figure 1. See Table 1 for parameters.

Note that since the radical signs in Eq. (S4) indicate the principal square root, $\mathrm{Re}(K^2_{1+}) > \mathrm{Re}(K^2_{1-})$ and $\mathrm{Re}(K^2_{0+}) > \mathrm{Re}(K^2_{0-})$. As we will show later, the fact that some K^2 are negative or complex is not a concern.

In order to impose the appropriate boundary conditions (i.e., the wavefunction must vanish at the lateral boundary, when the radial coordinate $\rho = R$) we must consider combinations of these K states.[33–35] The radial wavefunction for the state with momentum K is proportional to $J_\ell(K\rho)$, with the integer ℓ determined based on the total angular momentum F_z for a given basis vector through the relation $\ell = F_z - J_z$. The form of the wavefunction depends on which branch ($E^{1\pm}$ or $E^{0\pm}$) the K solution corresponds to (see Fig. 2). Written in the basis of Eq. (16), the forms for each branch are:

$$\langle \rho, \phi | E^{1\pm}(F_z, K) \rangle = \frac{e^{iF_z\phi}}{\sqrt{2\pi[1+(c_{1\pm}(K))^2]}} \begin{pmatrix} 0 \\ \frac{c_{1\pm}e^{-i\phi}}{\sqrt{2}} J_{F_z-1}(kK\rho) \\ J_{F_z}(K\rho) \\ \frac{c_{1\pm}e^{i\phi}}{\sqrt{2}} J_{F_z+1}(K\rho) \end{pmatrix},$$

(19)

$$\langle \rho, \phi | E^{0\pm}(F_z, K) \rangle = \frac{e^{iF_z\phi}}{\sqrt{2\pi[1+c_{0\pm}(K))^2]}} \begin{pmatrix} c_{0\pm} J_{F_z}(K\rho) \\ -\frac{e^{-i\phi}}{\sqrt{2}} J_{F_z-1}(kK\rho) \\ 0 \\ \frac{e^{i\phi}}{\sqrt{2}} J_{F_z+1}(K\rho) \end{pmatrix}.$$

(20)

The wavefunction for each K is determined by matching to the appropriate E branch. We label the wavefunctions $E^{1,1}$, $E^{1,2}$, $E^{0,1}$

and $E^{0,2}$ as follows:

$$\left| E^{1,1}(F_z) \right\rangle = \begin{cases} \left| E^{1+}(F_z, K_{1+}) \right\rangle & \text{if } E^{1+}(K_{1+}) = E \\ \left| E^{1-}(F_z, K_{1+}) \right\rangle & \text{if } E^{1-}(K_{1+}) = E \end{cases}$$

$$\left| E^{1,2}(F_z) \right\rangle = \begin{cases} \left| E^{1+}(F_z, K_{1-}) \right\rangle & \text{if } E^{1+}(K_{1-}) = E \\ \left| E^{1-}(F_z, K_{1-}) \right\rangle & \text{if } E^{1-}(K_{1-}) = E \end{cases}$$

$$\left| E^{0,1}(F_z) \right\rangle = \begin{cases} \left| E^{0+}(F_z, K_{0+}) \right\rangle & \text{if } E^{0+}(K_{0+}) = E \\ \left| E^{0-}(F_z, K_{0+}) \right\rangle & \text{if } E^{0-}(K_{0+}) = E \end{cases}$$

$$\left| E^{0,2}(F_z) \right\rangle = \begin{cases} \left| E^{0+}(F_z, K_{0-}) \right\rangle & \text{if } E^{0+}(K_{0-}) = E \\ \left| E^{0-}(F_z, K_{0-}) \right\rangle & \text{if } E^{0-}(K_{0-}) = E. \end{cases}$$

(21)

These four wavefunctions are orthogonal in the bulk. A linear combination of these states is the general wavefunction with energy E. As a result the total wavefunction of the state $|\psi_{F_z}\rangle$ with angular momentum projection F_z and energy E can be written as

$$|\psi_{F_z}\rangle = A \left| E^{1,1}(F_z) \right\rangle + B \left| E^{1,2}(F_z) \right\rangle + C \left| E^{0,1}(F_z) \right\rangle + D \left| E^{0,2}(F_z) \right\rangle.$$

(22)

We can now impose the boundary conditions. The wavefunction at the lateral boundary $\rho = R$ must vanish, i.e., $\left\langle R, \phi | \psi_{F_z} \right\rangle = 0$. This means that each line of the vector wavefunction must vanish at $\rho = R$, resulting in

$$\begin{pmatrix} C\frac{c_{0,1}J_{F_z}(K_{0+}R)}{\sqrt{1+c_{0,1}^2}} + D\frac{c_{0,2}J_{F_z}(K_{0-}R)}{\sqrt{1+c_{0,2}^2}} \\ -A\frac{c_{1,1}J_{F_z-1}(K_{1+}R)}{\sqrt{1+c_{1,1}^2}} - B\frac{c_{1,2}J_{F_z-1}(K_{1-}R)}{\sqrt{1+c_{1,2}^2}} + C\frac{J_{F_z-1}(K_{0+}R)}{\sqrt{1+c_{0,1}^2}} + D\frac{J_{F_z-1}(K_{0-}R)}{\sqrt{1+c_{0,2}^2}} \\ A\frac{J_{F_z}(K_{1+}R)}{\sqrt{1+c_{1,1}^2}} + B\frac{J_{F_z}(K_{1-}R)}{\sqrt{1+c_{1,2}^2}} \\ A\frac{c_{1,1}J_{F_z+1}(K_{1+}R)}{\sqrt{1+c_{1,1}^2}} + B\frac{c_{1,2}J_{F_z+1}(K_{1-}R)}{\sqrt{1+c_{1,2}^2}} + C\frac{J_{F_z+1}(K_{0+}R)}{\sqrt{1+c_{0,1}^2}} + D\frac{J_{F_z+1}(K_{0-}R)}{\sqrt{1+c_{0,2}^2}} \end{pmatrix} = 0, \quad (23)$$

where $c_{1,1}$, $c_{1,2}$, $c_{0,1}$, and $c_{0,2}$ are defined analogously to $E^{1,1}$, etc. in Eq. (S10). Redefining $A \equiv A/\sqrt{1+c_{1,1}^2}$, $B \equiv B/\sqrt{1+c_{1,2}^2}$, $C \equiv C/\sqrt{1+c_{0,1}^2}$, and $D \equiv D/\sqrt{1+c_{0,2}^2}$ and writing in matrix form,

$$\begin{pmatrix} 0 & 0 & c_{0,1}J_{F_z}(K_{0+}R) & c_{0,2}J_{F_z}(K_{0-}R) \\ -c_{1,1}J_{F_z-1}(K_{1+}R) & -c_{1,2}J_{F_z-1}(K_{1-}R) & J_{F_z-1}(K_{0+}R) & J_{F_z-1}(K_{0-}R) \\ J_{F_z}(K_{1+}R) & J_{F_z}(K_{1-}R) & 0 & 0 \\ c_{1,1}J_{F_z+1}(K_{1+}R) & c_{1,2}J_{F_z+1}(K_{1-}R) & J_{F_z+1}(K_{0+}R) & J_{F_z+1}(K_{0-}R) \end{pmatrix} \begin{pmatrix} A \\ B \\ C \\ D \end{pmatrix} = 0.$$

(24)

In order for there to be a nontrivial solution the determinant of the matrix must vanish. The energies E for which this is possible are the quantized energy levels due to lateral confinement. Having found these energies we can also find the coefficients A, B, C, and D to produce the wavefunction from Eq. (22), which we need in order to calculate properties such as the oscillator transition strength.

In some cases, quantum disk energy solutions can be found solely by mixing within the $E^{0\pm}$ or $E^{1\pm}$ branches, without cross-branch 0 to 1 mixing. That is, solutions exist which could be found by solving a determinantal equation for only one of the 2×2 blocks in Eq. (S18) rather than the full 4×4 determinantal equation. This only occurs when $F_z = 0$; for $F_z \neq 0$ branch decoupling is impossible. This is demonstrated in the Numerical Results section and a proof is provided in Sec. S-III of the ESI.

As noted earlier, K^2 may occasionally be negative or complex. It can be shown that there are nevertheless only 4 degrees of freedom in Eq. (24) so the problem remains solvable. Moreover, with the choice of an appropriate global phase, the wavefunctions at $\phi = 0$ are real. This may also be seen in the Numerical Results, and proofs are provided in ESI Sec. S-IV.

4 Oscillator transition strength

We can now calculate the oscillator transition strength f[36] of the confined states using the wavefunctions given by Eq. (22). In the ESI Sec. S-V we consider light with polarization vectors $\hat{e}_0 = \hat{z}$ and $\hat{e}_{\pm 1} = (\hat{x} \pm i\hat{y})/\sqrt{2}$. We define $f_\mu^{F_z}$ to be the oscillator strength for this polarization, that is, $f_{\pm 1}$ denotes the oscillator strength for circular polarized light propagating with wave vector along the $+\hat{z}$ direction, with positive (+) and negative (−) helicity, while f_0 denotes linearly polarized light with polarization vector along $\hat{z}$. We arrive at Eq. (S57), reproduced below:

$$f_0^{F_z} = 2\sin^2(\theta)\mathscr{K}_{F_z,0}^2 \left(\frac{E_p}{\hbar\omega}\right)\delta_{F_z,0} \ ,$$

$$f_{\pm 1}^{F_z} = \cos^2(\theta)\mathscr{K}_{F_z,\pm 1}^2 \left(\frac{E_p}{\hbar\omega}\right)\delta_{F_z,\pm 1} \ . \tag{25}$$

Here $\mathscr{K}_{F_z,\nu}$ is a dimensionless geometric integral defined in Eq. (S50), which is proportional to the area of the quantum disk. E_p is the Kane energy, $\hbar\omega$ is the transition energy, and the crystal-field-induced phase angle θ is defined in Eq. (S53). Since $\sin\theta$ is small (see Table 1), the oscillator strength $f_0 \ll f_{\pm 1}$. Note that the oscillator strength is only nonzero for exciton states with total angular momentum projection $F_z = 0$ and $F_z = \pm 1$.

Fieramosca *et al.* reported the oscillator strength per unit area of thin film samples of the 2D HOIP phenethylammonium lead iodide, $(C_6H_5(CH_2)_2NH_3)_2PbI_4$, commonly known as PEPI,[37] for polarization parallel to $(f_\parallel/A)$ and perpendicular to $(f_\perp/A)$ the inorganic layer with surface area A. These measurements allow us to extract an experimental value of E_p. In the bulk limit, Eq. (25) becomes

$$\left(\frac{f_\parallel}{A}\right) = \left(\frac{E_p}{\hbar\omega}\right)\cos^2\theta \left|\phi_{1,0}(0)\right|^2 \ ,$$

$$\left(\frac{f_\perp}{A}\right) = 2\left(\frac{E_p}{\hbar\omega}\right)\sin^2\theta \left|\phi_{1,0}(0)\right|^2 \ . \tag{26}$$

From the measured oscillator strength for in-plane versus out-of-plane polarizations we find,

$$\tan\theta = \sqrt{\frac{1}{2}\left(\frac{f_\perp/A}{f_\parallel/A}\right)} \ , \tag{27}$$

$$\left(\frac{E_p}{\hbar\omega}\right) = \frac{\pi a_{10}^2}{8}\frac{1}{\cos^2\theta}\left(\frac{f_\parallel}{A}\right) \ . \tag{28}$$

Using $a_{10} = 2.805$ nm, $(f/A)_\parallel = 4.4 \times 10^{13}$ cm^{-2}, and $f_\perp/f_\parallel = 0.16$ (see Table 1), we find $E_p/(\hbar\omega) = 1.468$. This is much smaller than the estimate $E_p/(\hbar\omega) = 3/m^*$ from a simple K.P model.[8] Additionally, Eq. (27) allows a cross-check of the crystal field phase

angle, which is $\theta = 0.276$ based on these quantities. This is in good agreement with the phase angle estimated from fine structure measurements $\theta = 0.229$[30] that we use in Table 1.

5 Long range exchange

Having written expressions for the transition oscillator strength for the confined states of the quasi-2D quantum disk, we are now in a position to calculate the LR exchange corrections to the energy.[9,23,32] In CGS units,

$$H_{F_z}^{LR} = \int_{V_1} dV_1 \int_{V_2} dV_2 \left[-\boldsymbol{\nabla}_1 \cdot \mathscr{P}_{F_z}(\boldsymbol{r}_1)\right]^* \frac{1}{\varepsilon_i |\boldsymbol{r}_1 - \boldsymbol{r}_2|}\left[-\boldsymbol{\nabla}_2 \cdot \mathscr{P}_{F_z}(\boldsymbol{r}_2)\right] \ . \tag{29}$$

where $\mathscr{P}_{F_z}$ is the transition dipole moment density associated with a given exciton state Ψ_{F_z} and ε_i is the dielectric function screening the Coulomb interaction inside the inorganic layer. Using the relation between matrix elements of the electric dipole and the momentum operators, $\langle 1|\hat{\boldsymbol{\mu}}|2\rangle = i(e\hbar/m_0)\langle 1|\hat{\boldsymbol{p}}|2\rangle/(E_2 - E_1)$ we can identify the polarization as proportional to the quantity that, when integrated, yields the transition dipole moment in Eq. (S47). This quantity is thus given by,

$$\mathscr{P}_{F_z}^\dagger = i\frac{\hbar e}{m_0\hbar\omega}\phi_{n,m}(0)\frac{\mathscr{N}}{\sqrt{2\pi}}\sum_\nu e^{i(F_z-\nu)\phi}\mathscr{R}_{1,\nu}^{F_z}(\rho)\langle\mathscr{G}|\hat{\boldsymbol{p}}|1,\nu\rangle \ . \tag{30}$$

Here, the unit cell transition momentum matrix elements $\langle\mathscr{G}|\hat{\boldsymbol{p}}|1,\nu\rangle$ are given in Eq. (S52) in terms of the Kane matrix element. Taking into account the finite thickness $\mathscr{L}$, we show in ESI Sec. S-VI that the polarization is given by

$$\mathscr{P}_{F_z}^\dagger = i\frac{P_{cv}\hbar e}{m_0\hbar\omega}\sum_\nu \mathscr{F}_{F_z,\nu}(\rho,\phi,z)\ \hat{\boldsymbol{n}}_\nu \ , \tag{31}$$

where we have defined the functions $F_{F_z,\nu}(\rho,\phi,z)$ in Eq. (S61). Inserting into Eq. (29) we have in CGS units,

$$H_{F_z}^{LR} = \frac{1}{\varepsilon_i}\left(\frac{P_{cv}\hbar e}{m_0\hbar\omega}\right)^2 \mathscr{J}_{F_z} \ , \tag{32}$$

where the LR exchange integral $\mathscr{J}_{F_z}$ is given by,

$$\mathscr{J}_{F_z} = \sum_{\nu,\nu'}\int_{V_1} dV_1 \int_{V_2} dV_2 \left[-\boldsymbol{\nabla}_1 \cdot \mathscr{F}_{F_z,\nu}(\rho_1,\phi_1,z_1)\hat{\boldsymbol{n}}_\nu\right]^* \frac{1}{|\boldsymbol{r}_1 - \boldsymbol{r}_2|}\times$$
$$\left[-\boldsymbol{\nabla}_2 \cdot \mathscr{F}_{F_z,\nu'}(\rho_2,\phi_2,z_2)\hat{\boldsymbol{n}}_{\nu'}\right] \ . \tag{33}$$

We can eliminate the Kane matrix element in Eq. (32) in favor of the oscillator strength per unit area measured in bulk 2D HOIP films or the bulk longitudinal-transverse splitting $\hbar\omega_{LT}$. Modeling a bulk 2D layered HOIP as a multi-quantum-well (i.e., with no electronic coupling between layers) in the long wavelength limit, the oscillator strength per volume V of the bulk layered material for excitons whose transition dipoles are polarized in the plane of the layers is given by the corresponding oscillator strength per unit area of an individual layer, $f_\parallel/A$, divided by the spacing, Λ, between sheets[38,39]:

$$\frac{f_\parallel}{V} = \left(\frac{E_p}{\hbar\omega}\right)g_{\pm 1}^2 \frac{|\phi_{1,0}(0)|^2}{\Lambda} \ , \tag{34}$$

where we have made use of Eq. (S52) defining $g_{\pm 1}$, Eq. (26) defining the oscillator strength per unit area per layer, and Eq. (S51) for the ground exciton relative wavefunction. One can see that in long wavelength limit Eq. (34) is the oscillator transition strength of a single QW multiplied by the QW density. The oscillator strength is in turn connected to the LT splitting for excitons whose transition dipoles are polarized in-plane. This is given in CGS units as, [40]

$$\hbar\omega_{LT}^{\parallel} = \frac{2\pi e^2 \hbar^2}{\tilde{\varepsilon}_\infty m_0 \hbar\omega} \frac{f_\parallel}{V} \approx \frac{2\pi e^2 \hbar^2}{\tilde{\varepsilon}_\infty m_0 E_g} \left(\frac{f_\parallel}{V}\right)_{\hbar\omega = E_g}, \qquad (35)$$

where we approximate the bulk exciton transition energy as the band gap, and where $\tilde{\varepsilon}_\infty$ is the high frequency *effective* dielectric constant of the medium, representing a volume weighted average of the dielectric constants inside and outside each layer. Eliminating terms we find,

$$H_{F_z}^{LR} = \frac{1}{4\pi} \frac{\tilde{\varepsilon}_\infty}{\varepsilon_i} \hbar\omega_{LT}^{\parallel} \left(\frac{E_g}{\hbar\omega}\right)^2 \frac{\Lambda}{g_{\pm 1}^2 |\phi_{1,0}(0)|^2} \mathscr{I}_{F_z}. \qquad (36)$$

It is useful to express the integral $\mathscr{I}_{F_z}$ in terms of the exchange overlap factor Θ and a dimensionless anisotropy function $\mathscr{A}_{F_z}$. These are defined as [8,9,23,41]:

$$\Theta = \Omega \iint_V d^3 r_e d^3 r_h \Psi_{F_z}^*(\boldsymbol{r}_e, \boldsymbol{r}_h) \delta(\boldsymbol{r}_e - \boldsymbol{r}_h) \Psi_{F_z}(\boldsymbol{r}_e, \boldsymbol{r}_h)$$

$$= \frac{3}{2\mathscr{L}} \Omega |\phi_{nm}(0)|^2. \qquad (37)$$

where Ω is the volume of the unit cell, and,

$$\mathscr{A}_{F_z} \equiv \frac{3}{4\pi} \frac{\Omega}{\Theta} \mathscr{I}_{F_z}. \qquad (38)$$

We note that, by construction, $\mathscr{A}_{F_z}$ is dimensionless; the integral $\mathscr{I}_{F_z}$ has dimensions of inverse volume. The final result is dependent on the inorganic layer thickness $\mathscr{L}$ and the disk radius R:

$$H_{F_z}^{LR}(\mathscr{L}, R) = \frac{\tilde{\varepsilon}_\infty}{\varepsilon_i} \hbar\omega_{LT}^{\parallel} \left(\frac{E_g}{\hbar\omega}\right)^2 \frac{\Lambda}{2\mathscr{L} g_{\pm 1}^2} \frac{|\phi_{nm}(0)|^2}{|\phi_{1,0}(0)|^2} \mathscr{A}_{F_z}, \qquad (39)$$

where $g_{\pm 1}^2 = \cos^2\theta$ is derived from Eq. (S52), reflects the crystal field, and is near unity. This equation represents a self-consistency relation for $H_{F_z}^{LR}$ via $\hbar\omega = E_g + E_{\text{bind}} + E_{F_z} + H_{F_z}^{LR}$, where E_{F_z} is the energy calculated in the absence of LR exchange. In our implementation, the self-consistency relation is solved iteratively, and the $\mathscr{A}$ integrals are performed using adaptive Monte Carlo integration via the VEGAS algorithm. [42,43]

Though the long-range exchange does not mix the bulk eigenstates, it shifts their energies and thus can in principle mix the confined states for a given radius. However, there is numerical evidence that this mixing will be negligible in our system. Firstly, we find the scale of the long-range interaction is 2.2-7.0 meV, much smaller than energy scales of confinement and short-range exchange (see Fig. S-2 in the ESI). Furthermore, the long-range exchange is not systematically different for the different branches, suggesting that it will have little effect on branch mixing. To provide additional support for this assumption, we directly calculated LR exchange matrix elements between a selected confined ground

Parameter	Value	Description & Source
$w = C\Theta$	12 meV	short-range exchange constant [29]
$\mathscr{L}$	0.6 nm	inorganic layer thickness [44]
Λ	1.6 nm	layer spacing [44]
Ω	0.216 nm^3	inorganic pseudocubic unit-cell volume [44]
ε_i	6.1	interior dielectric constant [22]
ε_o	1.9	exterior dielectric constant [45]
E_r^e	40 meV	electron Rashba energy [11]
E_r^h	10 meV	hole Rashba energy, K.P estimate [18]
μ	0.091m_0	exciton reduced effective mass [46]
E_g	2.625 eV	band gap [46]
$(f/A)_\parallel$	4.4×10^{13} cm^{-2}	in-plane oscillator strength [37]
$(f/A)_\perp$	7.0×10^{12} cm^{-2}	out-of-plane oscillator strength [37]
$\sin\theta$	0.227	crystal field phase angle [30]

Table 1 Material parameters used for numerical calculations. Further parameters that are derived from these values are given in ESI Table S-1.

state and five higher-lying excited states at the same QD size R and envelope angular momentum F_z. Though the off-diagonal elements did not vanish, the magnitudes were on average only 22% of the diagonal elements, much smaller than the energy separation between states, so the induced mixing will be minimal. Numerical tests also showed vanishing LR matrix elements between states with different F_z as expected by symmetry. We therefore treat the long-range exchange interaction as a first-order perturbation, and neglect any LR-exchange-mediated mixing of the confined states.

6 Numerical Results

In order to gain insight into the fine structure, we will specialize to parameters which roughly correspond to the exciton fine structure in the 2D HOIP, PEPI. Parameters and sources are tabulated in Table 1. Since we assume $\alpha_e > 0$ and $\alpha_h < 0$ [18] and $m_e = m_h$, we arrive at $\alpha_e = 183$ meV nm and $\alpha_h = -91.5$ meV nm. These and other derived parameters are shown in Table S-1 in the ESI.

Fig. 3 shows the energy levels of confined wavefunctions calculated using these parameters. Larger values of $|F_z|$ are qualitatively similar to $F_z = 2$ and so are not plotted here. As can be seen from Eqs. (19) and (20) using the identity $J_{-n}(x) = (-1)^n J_n(x)$, solutions with negative F_z mirror the corresponding positive F_z solutions, but with the spatial wavefunctions of the $|1,+1\rangle$ and $|1,-1\rangle$ components switched. As a result, states at F_z and $-F_z$ have identical energy levels and oscillator strengths, so we restrict our attention to $F_z \geq 0$.

The overall trend for all states is to decrease in energy with increasing R as expected due to quantum confinement. For all the states with $F_z \neq 0$, the solutions contain a mixture of the $E^{0\pm}$ and $E^{1\pm}$ branches. As a result, they exhibit level anti-crossings, which may be clearly seen in Fig. 3. By contrast, states with $F_z = 0$ can be branch decoupled, so a given state is either purely from $E^{0\pm}$ or
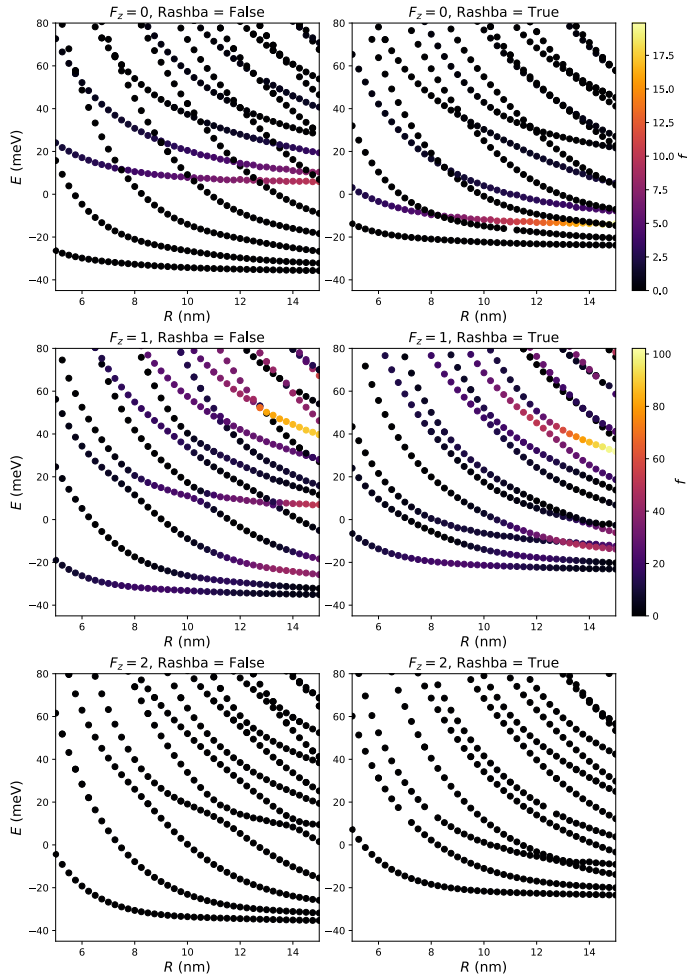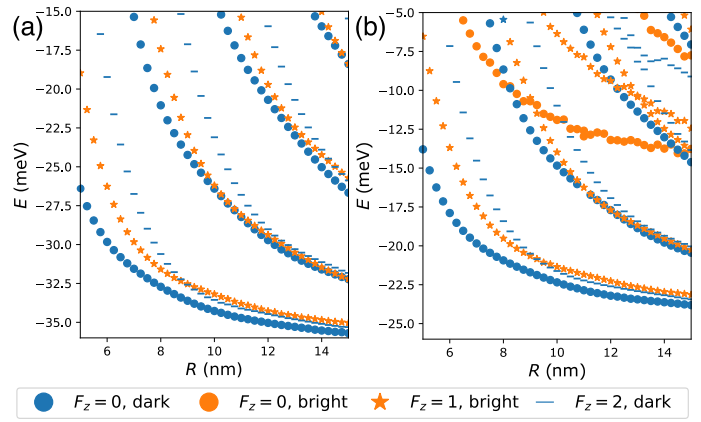
Fig. 4 Low-energy levels as a function of QD radius R, without (a) and with (b) internal Rashba. Color indicates whether the state is bright (optically active, shown in orange) or dark (optically passive, shown in blue) and shape indicates F_z (circles for $F_z = 0$, stars for $F_z = 1$, and lines for $F_z = 2$.) This subset of the data in Figure 3 is condensed here onto one plot for ease of comparison. Fluctuations in the bright $F_z = 0$ levels represent noise from the stochastic integration method used to calculate the long-range exchange.

Fig. 3 Energy levels of confined wavefunctions as a function of disk radius R. The columns show results calculated without internal Rashba on the left and with internal Rashba on the right. Rows are $F_z = 0$ (top), $F_z = 1$ (middle), and $F_z = 2$ (bottom). The total oscillator strength f of the states as given by Eq. (25) is indicated by the color of the points. Note the different color scale for $F_z = 0$ and $F_z = 1$.

$E^{1\pm}$. Two levels from opposite branches do not interact, so they do not exhibit anti-crossings, but instead act as two independent sets of levels, as seen in Fig. 3.

Low-energy states for $F_z = 0, 1, 2$ are shown in Figure 4. In small QDs, the situation is more typical of traditional exciton fine structure. The ground state is a dark $F_z = 0$ state, separated by several meV from bright states with $F_z = 0$ and $F_z = \pm 1$, with dark $|F_z| \geq 2$ states at higher energies. However, the fine structure of Rashba excitons in large quantum dots ($R \gtrsim 10$ nm) is quite different. The lowest-energy exciton states with $|F_z| \geq 2$ are comparable in energy to the $F_z = 0$ and $F_z = \pm 1$, quite close to the minimum energy of the bulk dispersion. Though only $F_z = 2$ is plotted in Figure 4, higher F_z also contribute states very close to the ground state, to an increasing degree as R increases. The implications of this proliferation of dark states will be discussed later.

Fig. 5 shows the total oscillator strength of the states, as given by Eq. (25). The $F_z = \pm 1$ states are the brightest states of the Rashba exciton. Only states with $F_z = 0, \pm 1$ have nonzero oscillator strength, and the $F_z = \pm 1$ oscillator strengths are proportional to $g_1 = \cos^2 \theta$, whereas $F_z = 0$ oscillator strengths are proportional to $g_0 = 2\sin^2 \theta$. Since $\theta \ll 1$, the $F_z = \pm 1$ states are brighter.

The oscillator strength is proportional to R^2 through the integral $\mathcal{K}$, and this broad trend can be seen in Figs. 3 and 5. However, the oscillator strength of a given state can also be observed to decrease with R in some circumstances. This occurs because shape of the wavefunction is also important to determine the oscillator strength. Wavefunctions with more nodes have a smaller oscillator strength, so a state's oscillator strength can decrease with increasing R as it develops an additional node. The oscillator strength's behavior is also somewhat unpredictable near avoided crossings where states with different oscillator strengths mix.

Additional qualitative features of the numerical results are illustrated with plots of the radial wavefunctions of various states in Fig. 6. In the figure, each panel corresponds to a distinct state;
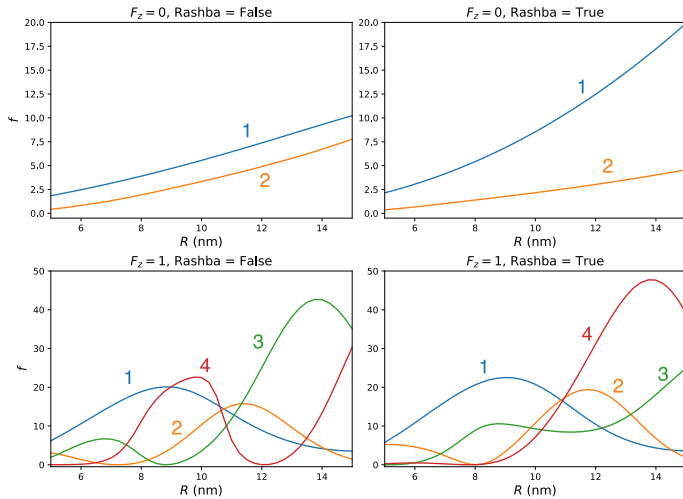
Fig. 5 Oscillator strengths of the low-energy states shown in Figure 3. The columns show results calculated without internal Rashba on the left and with internal Rashba on the right. The top row shows the oscillator strengths of the two lowest bright $F_z = 0$ states (both from the $E^{1\pm}$ branch since the states from the $E^{0\pm}$ branch have zero oscillator strength, see discussion in the text and Fig. 6). The bottom row shows the oscillator strengths of the four lowest $F_z = 1$ states.
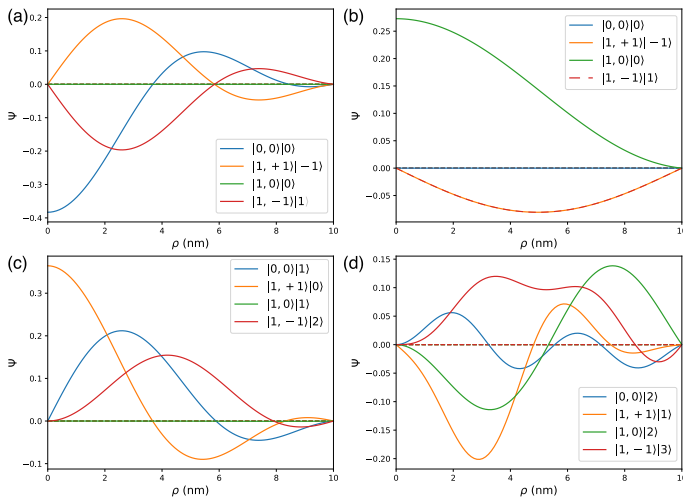

Fig. 6 Selected radial wavefunctions at $R = 10$ nm, without internal Rashba. Reported energies include LR exchange The four components of the total wavefunction are color coded, identified in the legend by the product form $|J, J_z\rangle|\ell\rangle$, where envelope angular momentum is denoted ℓ; see Eq. (22) and (20)-(19) (a) $F_z = 0$, $E = -34.3$ meV. Branch-decoupled E^{0-} solution. (b) $F_z = 0$, $E = 7.8$ meV. Branch decoupled E^{1-} solution. The $J_z = -1$ component is represented by a dashed line in the plot to reveal the identical $J_z = +1$ component. (c) $F_z = 1$, $E = -33.2$ meV. $K_{1\pm}^2$ are complex and $K_{0\pm}^2 > 0$. The branches appear to be decoupled given the small weight of the $|1, 0\rangle|1\rangle$ component, but they are not: This component is in fact non-zero and there is a small contribution of $K_{1\pm}^2$. (d) $F_z = 2$, $E = 52.0$ meV. A fairly typical higher-energy solution. The branches are strongly coupled.

the line plots within each panel show the radial wave functions of each separate component of the total wavefunction of that state, denoted in the legends according to the product $|J, J_z\rangle|\ell\rangle$ to which each radial component corresponds, where the envelope angular momentum is denoted ℓ; see Eq. (22) and (20)-(19). Panel (a) shows a branch-decoupled E^{0-} solution with $F_z = 0$ (for which decoupling is allowed). The $|1, 0\rangle|0\rangle$ component does not contribute at all, while the $|1, \pm1\rangle|\mp1\rangle$ components have opposite sign, as expected from Eq. (20). This state has identically zero oscillator strength, as can be seen from Eq. (S50). Panel (b) shows a branch-decoupled E^{1-} solution. Here the $|0, 0\rangle|0\rangle$ component has zero weight while the $|1, \pm1\rangle|\mp1\rangle$ components have the same sign, again as expected from Eq. (19). This state has non-zero oscillator strength. Panel (c) illustrates a case of complex K^2, as discussed in ESI Sec. S-IV. Though the small weight of the $|1, 0\rangle|1\rangle$ component may visually suggest that this is a decoupled state, both branches do in fact contribute to this state, and the wavefunctions are real. Panel (d) shows a typical example of a high-energy solution with complex node structure in which neither branch is dominant.

Discussion

We have found analytical expressions describing the energy dispersion of Rashba excitons in 2D perovskite structures with tetragonal symmetry, which take into account short-range and long-range exchange interactions and Rashba spin-orbit terms acting on electrons and holes. Placing these excitons into quasi-2D cylindrical quantum dots, we calculate the size dependence of the energies of the exciton confined levels and their oscillator transition strengths. Although the parameters used for the numerical calculations were chosen to correspond to the 2D HOIP PEPI,[11,18,22,29,30,37,44–46] the developed theory is very general and can be applied to any 2D perovskite layer with arbitrary sign and magnitude of the Rashba coefficients, or indeed to any 2D semiconductor layer with parabolic dispersion, tetragonal symmetry, and Rashba terms with inversion asymmetry along the out-of-plane axis. Generalizability is facilitated by the provided python code,[†] which allows the user to vary the parameters freely and calculate the resulting dispersion and confined level structure. A PEPI analogue with an increased number of inorganic layers or longer organic spacer cations can easily be treated by tuning the layer thickness $\mathscr{L}$ and/or inter-layer spacing Λ as appropriate. Other 2D HOIPs can be modeled through the use of appropriate material properties, either calculated from first principles or measured experimentally. The model is also applicable in the complete absence of lateral confinement (i.e., the 2D quantum well limit), in which the exciton level structure is given by the dispersion at $K = 0$ in (16) and the wavefunctions are given by Eq. (17).

The main unusual feature of Rashba exciton dispersion (see Fig. 1) is the dispersion minimum, previously predicted in,[17] which has a cylindrical shape and occurs at quasi momentum $|K_R| \neq 0$. While excitons connected with this minimum are optically inactive, phonon-assisted transitions to the dark states may still appear in optical absorption and photoemission experiments in 2D HOIPs. As we have shown in Eq. (S9), this minimum has

an effective 1D density of states $D(E)$, diverging as $1/\sqrt{E - \mathscr{E}_{\min}}$ as the exciton energy E approaches the exciton energy minimum $\mathscr{E}_{\min}$. Such dispersion of the free exciton significantly enhances the phonon-assisted transition rates (see Eq. (18)) and indicates that in absorption experiments one may observe multiple phonon-assisted lines connected with creation of excitons with $\boldsymbol{K}_R \neq 0$ in addition to the three optically allowed excitons at $K = 0$. At low temperatures the excitons should relax to this minimum. Their photoluminescence would be seen as multiple acoustic- and/or optical-phonon-assisted transitions, separated by differences in the phonon energies. Indeed, the Rashba exciton's dark states both associated with the exciton Bloch functions and the indirect minimum, may therefore explain multiple excitonic lines observed in 2D HOIPs. [47–49] Another important consequence of the 1D density of states of the Rashba exciton is the resulting enhanced localization of shallow defects and impurities. [50]

The level structure and oscillator transition strengths of Rashba excitons confined in a 2D cylindrical quantum dot are quite unusual. One notable aspect of the level structure is the proliferation of dark exciton states. In small quantum dots ($R \lesssim 8$ nm), the model reproduces the expected behavior based on previous perturbative treatments and the exciton fine structure is qualitatively similar to an exciton in parabolic-band perovskite nanocrystals, [8,23] with an $F_z = 0$ dark ground state, first excited states that are optically active with $F_z = \pm 1$, followed by the first optically active state with $F_z = 0$. All these exciton energies are proportional to $1/R^2$ with the same constant of proportionality (see ESI Fig. S-4). At larger sizes, the dispersion becomes more complicated, but the ground state $F_z = 0$ remains dark (see Figure 4). However the dark states with high angular momentum $|F_z| > 1$ become comparable in energy to the $F_z = 0$ ground state, appearing below the $F_z = \pm 1$ bright states. The proliferation of dark states may be difficult to detect optically or to disentangle from the $F_z = 0$ ground state, making experimental probes of the detailed fine structure challenging. These dark states in large quantum dots are also likely to be thermally populated even at fairly low temperatures, reducing the radiative decay rate and consequently the PL quantum yield of these structures. Magneto-optical study of the quantum dot PL could provide experimental identification and characterization of high-F_z dark exciton states.

While the present work focuses on two-dimensional quantum dots, the obtained results could be qualitatively applied to 3D nanocrystals. This theory can be used in cases when the perturbation theory described in Refs 4,8 is not valid, such as NCs with a very large Rashba coefficient or very large NCs with a moderate Rashba coefficient. For example, a cube-shaped CsPbBr$_3$ NC with side length greater than 20 nm and Rashba coefficients $\alpha_e \approx \alpha_h \approx 0.4$ eV Å would be outside the perturbative regime and can be productively explored using the Rashba exciton model. The theory also applies whether the electron and hole Rashba coefficients have different signs (as assumed here for PEPI) or the same sign (as assumed in previous work on CsPbBr$_3$ [4,8]). The two cases for the relative sign are compared in ESI Fig. S-4. For rather small QDs in the same-sign case, the ground exciton state is bright, but its oscillator transition strength decreases with increasing QD radius R. The lowest exciton energy levels also approach

the minimum of the exciton dispersion. Due to the large wave vector of the bulk excitons at this minimum, the ground states of confined excitons therefore comprise standing waves with multiple radial nodes, and in large QDs radiative recombination of the ground state becomes, not spin forbidden, but momentum forbidden. This exact 2D analysis can be qualitatively applied to 3D NCs, suggesting that the indirect minimum of the exciton dispersion in the plane perpendicular to the broken NC symmetry would create a momentum-forbidden dark exciton in large NCs regardless of the relative sign of the electron and hole Rashba coefficients.

In the ongoing search for bright ground excitons, an improved understanding of the exciton structure provided by the Rashba exciton model is vital. For a Rashba exciton, a bright-dark inversion at $K = 0$ is not sufficient to produce a ground bright exciton in a QD if the global dispersion minimum is still a momentum-forbidden dark state. However, according to our model, a bright ground state can arise in two ways. Firstly, if the Rashba coefficients α_e and α_h have the same sign, the center-of-mass terms lead to a bright ground state at intermediate confinement, just as in previous perturbative models, [4,8] but at significantly smaller QD sizes. This is shown in ESI Fig. S-4, which shows that the ground state is bright but with a small oscillator strength that peaks around $R = 4$ nm. Alternatively, if α_e and α_h have opposite sign, a stronger short-range exchange interaction could create a bright ground state of the global exciton dispersion at $K = 0$. This will lead to a bright ground state in sufficiently large QDs. For example, if we use the parameters from Table 1 except set $w = 30$ meV, a value representative of PbBr$_4$-based 2D HOIPs, [31] the minimum of the dispersion is a bright E^{1-} state, and the $F_z = 0$ ground state for excitons confined in a cylindrical QD for $R \gtrsim 12$ nm is bright (see Supplementary Figure S-5). Therefore, we suggest expanding the search for bright ground excitons in 2D materials such as HOIPs, paying special attention to systems with strong electron-hole exchange interactions (such as the bromide systems) or in which α_e and α_h have the same sign.

Author Contributions

Conflicts of interest

There are no conflicts to declare.

Acknowledgments

Notes and references

1 M. Nirmal, D. J. Norris, M. Kuno, M. G. Bawendi, Al. L. Efros and M. Rosen, *Phys. Rev. Lett.*, 1995, **75**, 3728–3731.

2 L. Protesescu, S. Yakunin, M. I. Bodnarchuk, F. Krieg, R. Caputo, C. H. Hendon, R. X. Yang, A. Walsh and M. V. Kovalenko, *Nano Lett.*, 2015, **15**, 3692–3696.

3 G. Rainò, G. Nedelcu, L. Protesescu, M. I. Bodnarchuk, M. V. Kovalenko, R. F. Mahrt and T. Stöferle, *ACS Nano*, 2016, **10**, 2485–2490.

4 M. A. Becker, R. Vaxenburg, G. Nedelcu, P. C. Sercel, A. Shabaev, M. J. Mehl, J. G. Michopoulos, S. G. Lambrakos, N. Bernstein, J. L. Lyons, T. Stöferle, R. F. Mahrt, M. V. Kovalenko, D. J. Norris, G. Raino and Al. L. Efros, *Nature*, 2018, **553**, 189–193.

5 A. Liu, D. B. Almeida, L. G. Bonato, G. Nagamine, L. F. Zagonel, A. F. Nogueira, L. A. Padilha and S. Cundiff, *Sci. Adv.*, 2021, **7**, eabb3594.

6 P. Tamarat, M. I. Bodnarchuk, J.-B. Trebbia, R. Erni, M. V. Kovalenko, J. Even and B. Lounis, *Nat. Mater.*, 2019, **18**, 717–724.

7 P. Tamarat, L. Hou, J.-B. Trebbia, A. Swarnkar, L. Biadala, Y. Louyer, M. I. Bodnarchuk, M. V. Kovalenko, J. Even and B. Lounis, *Nat. Commun.*, 2020, **11**, 6001.

8 P. C. Sercel, J. L. Lyons, D. Wickramaratne, R. Vaxenburg, N. Bernstein and Al. L. Efros, *Nano Lett.*, 2019, **19**, 4068–4077.

9 P. C. Sercel, J. L. Lyons, N. Bernstein and Al. L. Efros, *J. Chem. Phys*, 2019, **151**, 234106.

10 X. Liu, A. Chanana, U. Huynh, F. Xue, P. Haney, S. Blair, X. Jiang and Z. V. Vardeny, *Nat. Commun.*, 2020, **11**, 323.

11 Y. Zhai, S. Baniya, C. Zhang, J. Li, P. Haney, C.-X. Sheng, E. Ehrenfreund and Z. V. Vardeny, *Sci. Adv*, 2017, **3**, e1700704.

12 M. Jana, R. Song, Y. Xie, R. Zhao, P. Sercel, V. Blum and D. Mitzi, *Nat. Commun.* (accepted), 2021, DOI: 10.21203/rs.3.rs-472412/v1.

13 M. K. Jana, R. Song, H. Liu, D. R. Khanal, S. M. Janke, R. Zhao, C. Liu, Z. V. Vardeny, V. Blum and D. B. Mitzi, *Nat. Comm.*, 2020, **11**, 1–10.

14 F. Wang, H. Gao, C. de Graaf, J. M. Poblet, B. J. Campbell and A. Stroppa, *npj Computational Materials*, 2020, **6**, 1–8.

15 Al. L. Efros and L. E. Brus, *ACS Nano*, 2021, **15**, 6192–6210.

16 P. Geiregat, C. Rodá, I. Tanghe, S. Singh, A. Di Giacomo, D. Lebrun, G. Grimaldi, J. Maes, D. Van Thourhout, I. Moreels *et al.*, *Light: Science & Applications*, 2021, **10**, 1–11.

17 P. C. Sercel, Z. V. Vardeny and Al. L. Efros, *Nanoscale*, 2020, **12**, 18067–18078.

18 P. C. Sercel, *Theory of excitons in metal halide perovskites*, World Scientific Publishing Company, USA, 2021.

19 N. C. Ritova, *Vestnik of Moskow University*, 1967, **N3**, 30.

20 L. V. Keldish, *JETP Lett.*, 1979, **29**, 716–719.

21 E. Hanamura and N. Nagaosa, *Mater. Sci. Eng. B*, 1988, **1**, 255–258.

22 X. Hong, T. Ishihara and A. U. Nurmikko, *Phys. Rev. B.*, 1992, **45**, 6961–6964.

23 M. Gramlich, M. W. Swift, J. L. Lyons, Al. L. Efros, P. C. Sercel and A. Urban, (submitted).

24 X. L. Yang, S. H. Guo, F. T. Chen, K. W. Wong and W. Y. Chin, *Phys. Rev. A*, 1991, **43**, 1186–1196.

25 R. R. Guseinov, *phys. stat. sol. (b)*, 1984, **125**, 237–243.

26 Y. Cho and T. C. Berkelbach, *J. Phys. Chem. Lett.*, 2019, **10**, 6189–6196.

27 J. C. Blancon, A. V. Stier, H. Tsai, W. Nie, C. C. Stoumpos, B. Traoré, L. Pedesseau, M. Kepenekian, F. Katsutani, G. T. Noe, J. Kono, S. Tretiak, S. A. Crooker, C. Katan, M. G. Kanatzidis, J. J. Crochet, J. Even and A. D. Mohite, *Nat. Commun.*, 2018, **9**, 1–10.

28 Y. Nagamune, S. Takeyama and N. Miura, *Phys. Rev. B*, 1991, **43**, 12401–12405.

29 K. Tanaka, K. T. Takahashi, T., K. Umeda, K. Ema, T. Umebayashi, K. Asai, K. Uchida and N. Miura, *Jpn. J. Appl. Phys., Part 2*, 2005, **44**, 5923–5932.

30 T. Kataoka, T. Kondo, R. Ito, S. Kazuhito, K. Uchida and N. Miura, *Phys. Rev. B*, 1993, **47**, 2010–2018.

31 K. Ema, K. Umeda, M. Toda, C. Yajima, Y. Arai and H. Kunugita, *Phys. Rev. B*, 2006, **73**, 241310(R).

32 K. Cho, *J. Phys. Soc. Japan*, 1999, **68**, 683–691.

33 E. N. Bulgakov and A. F. Sadreev, *Jetp Lett.*, 2001, **73**, 505–509.

34 Al. L. Efros and M. Rosen, *Phys. Rev. B*, 1998, **58**, 7120–7135.

35 P. C. Sercel and K. J. Vahala, *Phys. Rev. B*, 1990, **42**, 3690–3710.

36 Al. L. Efros and A. L. Efros, *Sov. Phys. Semicond.*, 1982, **16**, 772.

37 A. Fieramosca, L. D. Marco, M. Passoni, L. Polimeno, A. Rizzo, B. L. T. Rosa, G. Cruciani, L. Dominici, M. D. Giorgi, G. Gigli, L. C. Andreani, D. Gerace, D. Ballarini and D. Sanvitto, *ACS Photonics*, 2018, **5**, 4179–4185.

38 E. L. Ivchenko and G. E. Pikus, *Superlattices and Other Heterostructures: Symmetry and Optical Phenomena*, Springer-Verlag, Heidelberg, Germany, 2nd edn, 1997.

39 L. C. Andreani, *Phys. Lett. A*, 1994, **192**, 99–109.

40 L. C. Andreani and F. Bassani, *Phys. Rev. B*, 1990, **41**, 7536–7544.

41 B. D. Folie, J. A. Tan, J. Huang, P. C. Sercel, M. Delor, M. Lai, J. L. Lyons, N. Bernstein, Al. L. Efros, P. Yang and N. S. Ginsberg, *J. Phys. Chem. A*, 2020, **124**, 1867–1876.

42 G. Peter Lepage, *J. Comput. Phys.*, 1978, **27**, 192–203.

43 G. P. Lepage, *J. Comput. Phys.*, 2021, **439**, 110386.

44 K. Shibuya, M. Koshimizu, F. Nishikido, H. Saito and S. Kishimoto, *Acta Cryst.*, 2009, **E65**, m1323–m1324.

45 Y. Wei, *PhD thesis*, École normale supérieure de Cachan; East

China normal university (Shanghai), 2013.

46 M. Dyksik, S. Wang, W. Paritmongkol, D. K. Maude, W. A. Tisdale, M. Baranowski and P. Plochocka, *J. Phys. Chem. Lett*, 2021, **12**, 1638–1643.

47 F. Thouin, A. R. Srimath Kandada, D. A. Valverde-Chávez, D. Cortecchia, I. Bargigia, A. Petrozza, X. Yang, E. R. Bittner and C. Silva, *Chem. Mater.*, 2019, **31**, 7085–7091.

48 D. B. Straus, S. Hurtado Parra, N. Iotov, Q. Zhao, M. R. Gau, P. J. Carroll, J. M. Kikkawa and C. R. Kagan, *ACS Nano*, 2020, **14**, 3621–3629.

49 T. T. H. Do, A. Granados del Águila, J. Xing, S. Liu and Q. Xiong, *J. Chem. Phys.*, 2020, **153**, 064705.

50 M. E. Raikh and Al. L. Efros, *JETP Lett.*, 1988, **48**, 220–225.